

Searching new topological superfluids and phase transitions with spin-orbit coupled fermions in an optical lattice

Yu Yi-Xiang^{1,2}, Fadi, Sun^{1,3}, Jinwu Ye^{1,3} and Ningfang Song²

¹ *Department of Physics and Astronomy, Mississippi State University, P. O. Box 5167, Mississippi State, MS, 39762*

² *School of Instrument Science and Opto-electronics Engineering,*

Institute of Optics and Electronics, BeiHang University, Beijing 100191, China

³ *Department of Physics, Capital Normal University,*

Key Laboratory of Terahertz Optoelectronics, Ministry of Education,

and Beijing Advanced innovation Center for Imaging Technology, Beijing, 100048, China

(Dated: September 22, 2016)

We study the global phase diagram of attractively interacting fermions hopping in a square lattice with any linear combinations of Rashba or Dresselhaus spin-orbit coupling (SOC) in a normal Zeeman field. This is one of the simplest and most promising experimental setups to search for topological superfluids and associated Majorana fermions in cold atom systems. Here, we focus on half filling case. By imposing self-consistence equations, we find there are 3 phases Band insulator (BI), Superfluid (SF) and Topological SF with Chern number $C = 2$. The TSF happens in small Zeeman fields and very weak interactions which is the experimentally most easily accessible regimes and has also the smallest heating effects. The transition from the BI to the SF is a first order one due to the multi-minima structure of the energy landscape. There is a topological phase transition from the SF to the TSF at the low critical field h_{c1} , then another one from the TSF to the BI at the upper critical field h_{c2} . We derive effective actions to describe the two topological phase transitions, then study the edge modes and the Majorana zero modes inside a vortex core of the $C = 2$ TSF near both h_{c1} and h_{c2} , especially explore their spatial and spin structures. We map out the local Berry Curvature distribution near both h_{c1} and h_{c2} . We find a topological tri-critical point along h_{c1} and conjecture that any topological transitions can only be odd order. We also study some interesting bulk-Berry curvature-edge-vortex correspondences. Experimental implications such as heating issue, temperature requirements and detections of these new topological phenomena are discussed.

Topological phases and phase transitions has been under extensive investigations in various contexts such as quantum Hall effects¹, various fermionic systems², topological insulators and topological superconductors^{3,4} and also topological spin liquids^{5,6}. The scaling functions across the TQPT driven by SOC in a honeycomb lattice was studied in⁷. In this work, we study the topological phases and phase transition of attractively interacting fermions at half filling subject to the Rashba spin-orbit coupling (SOC) hopping in a square lattice in a normal Zeeman field Eq.1. This system has been previously looked at in⁸ and found to be a promising system to search for topological superfluid (TSF) in cold atom systems. Unfortunately, the self-consistent equations were ignored in⁸, so what are the ground states and phase transitions can not be determined, possible experimental implications are rather limited. Its counterpart in materials and in the continuum limit was studied in the s-wave superconductor- noncentro-symmetric semiconductor- magnetic insulator (SM-SC-MI) hetero-structure⁹. In this SC-SM-MI hetero-structure, the noncentro-symmetric SM hosts a strong Rashba or Dresselhaus SOC, the superconductor provides the S-wave pairing to the SM due to its proximity effects, the MI induces a Zeeman field applied to the SM. Under the combined effects of the SOC, S-wave paring and the Zeeman field, the SM sandwiched between the SC and MI may enter into a TSF phase which hosts Majorana fermions in its vortex core. In order to avoid unwanted orbital ef-

fects, an alternative setup with the SM in the proximity to an s-wave superconductor subject to an in-plane magnetic field was proposed in¹⁰. In the cold atom systems¹¹, it is difficult to construct such a hetero-structure, but one advantage over the structure is the absence of any orbital effects due to the charge neutrality of the cold atoms. Another big advantage is that all relevant parameters are experimentally tunable. A negative interaction $-U$ can be induced by a S-wave Feshbach resonance¹⁷. The Rashba SOC and the Zeeman field h can be generated by various Raman laser or optical lattice clock schemes¹²⁻¹⁶. The number of atoms N can be easily controlled. A crucial question to ask is what are the experimental conditions to observe possible TSF in such a cold atom system? If so, what are the properties of the TSF and associated topological phase transitions? To answer these questions, one must impose the self-consist equations under the tunable experimental parameters such as the SOC strength and the parameters N, U, h to determine the ground states and phase transitions, which can be directly detected with various techniques established in the cold atom experiments²⁰⁻²⁵. We will try to achieve this goal in this paper.

As shown in this paper, it is very important to impose the self-consistency conditions which lead to the global phase diagram in Fig.1. For the isotropic Rashba limit $\alpha = \beta$, there are three phases: a topological superfluid phase (TSF) at a small h and small U , a Band insulator (BI) at a large h and a normal SF at a large U . The

transition from the BI to the SF at $h = h_b$ is a bosonic one with the pairing amplitude Δ as the order parameter. It is a first order one with meta-stable regimes on both sides of the transition (denoted by the two dashed lines) in Fig.1. The topological transition from the SF to the TSF at $h = h_{c1}$ in Fig.1 is a fermionic one at the two Dirac points $(\pi, 0)$ and $(0, \pi)$ with no order parameter. It is a third order TQPT in the first segment along h_{c1} , then turn into a first order one at the topological tri-critical point T , continue to the multi-critical point M . The transition from the TSF to the BI at h_{c2} has both bosonic and fermionic nature, the bosonic sector has the pairing amplitude Δ as the order parameter representing the onset of the off-diagonal long range order of the TSF, the fermionic sector happens at the two Dirac points $(0, 0)$ and (π, π) with no order parameters, representing the onset of the topological nature of the TSF with $C = 2$. The two sectors become critical at the same time at $h = h_{c2}$. The distributions of the Berry curvature of the $C = 2$ TSF moves from sharply peaked at $(0, \pi)$ and $(\pi, 0)$ near h_{c1} in Fig.3a to be located around $(0, 0)$ and (π, π) near h_{c2} with the non-trivial structure shown in Fig.4a. In the TSF, there are always $C = 2$ Majorana edge modes at $k_y = 0$ and $k_y = \pi$ respectively which decay into the bulk with possible oscillating behaviors. The two Majorana edge modes carry both spins near h_{c1} , but spin up and spin down at $k_y = 0$ and $k_y = \pi$ respectively near h_{c2} . There are also $C = 2$ Majorana zero modes inside a vortex core which also show different spin structures near h_{c1} and h_{c2} . We explore interesting bulk energy spectrum-Berry curvature-edge state-vortex core relations.

We consider the Hamiltonian of interacting two pseudo-spin (labeled as \uparrow and \downarrow) fermions hopping in the 2D square lattice subject to any linear combinations of Rashba and Dresselhaus SOC and a Zeeman field:

$$H = -t \sum_i \left[c_i^\dagger e^{i\alpha\sigma_x} c_{i+\hat{x}} + c_i^\dagger e^{i\beta\sigma_y} c_{i+\hat{y}} + h.c. \right] - \mu \sum_i c_i^\dagger c_i - h \sum_i c_i^\dagger \sigma_z c_i + \frac{U}{L_x L_y} \sum_i c_{i\uparrow}^\dagger c_{i\downarrow}^\dagger c_{i\downarrow} c_{i\uparrow} \quad (1)$$

where $c_i^\dagger = \begin{bmatrix} c_{i\uparrow}^\dagger & c_{i\downarrow}^\dagger \end{bmatrix}$, $\sigma_{x,y,z}$ are three Pauli matrices, and \hat{x} and \hat{y} denote the unit vector in x and y direction respectively. The negative interaction $U < 0$ can be tuned by the Feshbach resonance. The chemical potential μ should be determined by the filling factor $\nu = \frac{N}{2L_x L_y}$, where N is the number of fermions, L_x (or L_y) is the size of the system along x (or y) direction, and the factor 2 comes from the two spin species.

In the following, we describe Fig.1 in the clockwise version: from the BI to the SF at h_b , then to the TSF at h_{c1} , then back to the BI at h_{c2} .

2. Exact symmetry analysis and qualitative physical pictures

Obviously, the Zeeman field breaks the Time reversal symmetry. As usual, there is always a P-H symmetry on the BCS mean field Hamiltonian Eq.A2: $CH_{MF}(\mathbf{k})C^- =$

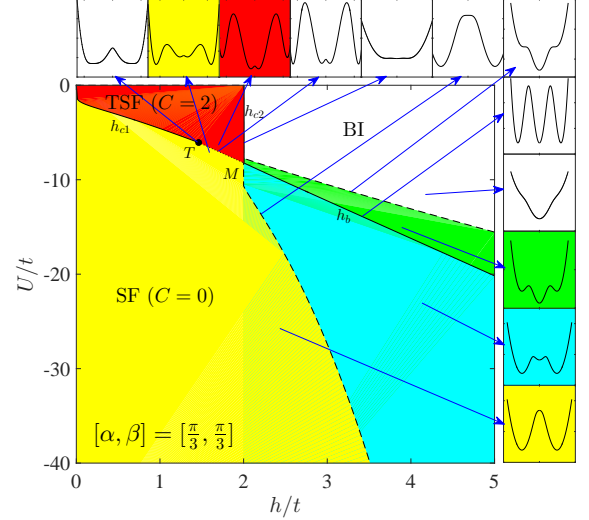


FIG. 1. (Color online) The global phase diagram in the parameter space of U and h at $[\alpha, \beta] = [\frac{\pi}{3}, \frac{\pi}{3}]$. The insets are the ground state energy E_G versus the bosonic SF order parameter Δ at each phase and phase boundary. At the BI to the SF phase boundary h_b , the three minima at 0 and $\pm\Delta$ become degenerate, so it is a first order one. The transition is a bosonic one with the superfluid order parameter Δ . Along h_{c1} , the SF to the TSF transition is third order between 0 and the topological Tri-critical point (T), then become first order between the T and the multi-critical point (M) where the four SF minima $\pm\Delta_+$ and $\pm\Delta_-$ become degenerate. The SF to TSF transition is a fermionic one with a topological feature, but no order parameters. The transition from the TSF to the BI at h_{c2} has both bosonic and fermionic (topological) nature. The three lines h_{c1} , h_{c2} and h_b meet at the multi-critical point M . The h_{c2} is strictly straight, while h_{c1} is tangent to $h = 0$ axis near the origin.

$-H_{MF}(-\mathbf{k})$ which picks up the four P-H invariant momenta $(0, 0)$, $(\pi, 0)$, $(0, \pi)$, (π, π) . The Hamiltonian Eq.1 also has the \mathcal{P}_z symmetry: $k_x \rightarrow -k_x$, $S^x \rightarrow -S^x$, $k_y \rightarrow -k_y$, $S^y \rightarrow -S^y$, $S^z \rightarrow S^z$ which is also equivalent to a joint π rotation of the spin and orbital around \hat{z} axis³¹. This symmetry indicates $\sigma_z H(\mathbf{k}) \sigma_z = H(-\mathbf{k})$. It also picks up the same four \mathcal{P}_z symmetric momenta²⁶. At the isotropic Rashba limit $\alpha = \beta$, it has the enlarged $[C_4 \times C_4]_D$ symmetry which is also equivalent to a joint $\pi/2$ rotation of the spin and orbital around \hat{z} axis. This symmetry indicates the equivalence between $(0, \pi)$ and $(\pi, 0)$. The Hamiltonian is also invariant under $\alpha \rightarrow \pi - \alpha$, $k_x \rightarrow \pi - k_x$ and $\beta \rightarrow \pi - \beta$, $k_y \rightarrow \pi - k_y$. At the extremely anisotropic limit ($\alpha = \pi/2, \beta$), it indicates the equivalence between $(0, 0)$ and $(\pi, 0)$, also between $(0, \pi)$ and (π, π) .

By introducing the superfluid order parameter Δ , we performed the mean field calculations on the Hamiltonian Eq.1 and imposed the self consistent equations to determine μ and Δ given N and (h, U) . The details are given in the appendix A. In this manuscript, we only focus on

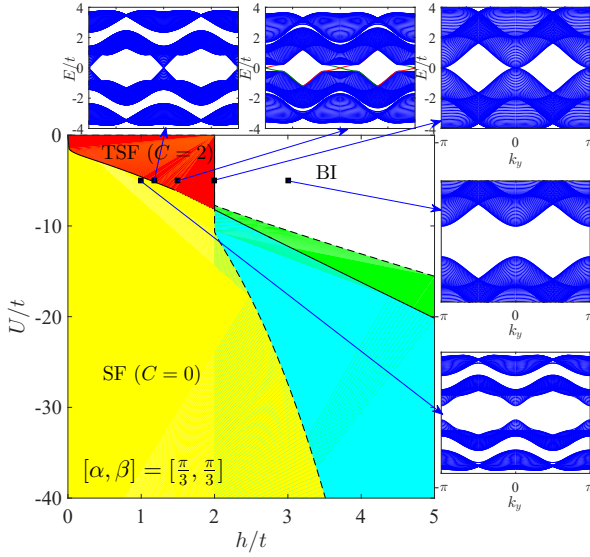


FIG. 2. (Color online) The fermionic quasi-particle excitations in different phases in Fig.1. Clockwise, their energies versus the momentum k_y (a) Along h_{c1} before hitting the topological Tri-critical point, there are two bulk gapless Dirac points at $(0, \pi)$ and $(\pi, 0)$ (b) TSF with $C = 2$ and its two edge states at $k_y = 0, \pi$. (c) Along h_{c2} , there are quadratic band touching at $(0, 0)$ and (π, π) (d) In the BI, there is a band gap due to the Zeeman field (e) In the SF, there is a quasi-particle gap due to the pairing. The edge state in the TSF in (b) is calculated under the open boundary conditions along x direction. The topological transition from the SF and TSF between the T and M point along h_{c1} is first order, so the quasi-particle excitations are gapped on both sides along this segment (not shown in the figure).

the half-filling case $\mu = 0$. At the half filling $\mu = 0$, the spectrum Eq.A4 has the symmetry $E(\mathbf{k}) = E[(\pi, \pi) + \mathbf{k}]$ which indicates the energies at the four momenta split into two groups $(0, 0), (\pi, \pi)$ and $(0, \pi), (\pi, 0)$. At the extremely anisotropic limit ($\alpha = \pi/2, \beta$), the energies at the two groups become degenerate. Any deviation from the anisotropic limit splits the 4 degenerate minima into the two groups which opens a window for the TSF. The TSF window reaches maximum at the isotropic Rashba limit $\alpha = \beta$ where the symmetry is enlarged to $[C_4 \times C_4]_D$. The main results for $\mu = 0$ are shown in Fig.1 and Fig.2. Here we only present the main physical pictures, especially possible topological transitions driven by the gap closing of fermionic excitations.

Indeed, at $\mu = 0$, $\xi^2(\mathbf{k}_0)$ in Eq.A7 split into two groups: $\xi^2(0, 0) = \xi^2(\pi, \pi) = 4t^2(\cos \alpha + \cos \beta)^2 > \xi^2(0, \pi) = \xi^2(\pi, 0) = 4t^2(\cos \alpha - \cos \beta)^2$. If neither α nor β equals to $\frac{\pi}{2}$, the two groups take two different values which could divide the system into 3 different phases: SF, TSF and BI phase. At $h < h_{c1}$, it is in a trivial SF phase where the fermionic excitation energy $E_{\mathbf{k}-}$ is gapped in the bulk with no edge states (Fig.2e). There is a SF to TSF transition at $h_{c1} = \sqrt{\xi^2(0, \pi) + \Delta^2}$ where the $E_{\mathbf{k}-}$ touches zero linearly and simultaneously at the two

Dirac points at $\mathbf{k} = (\pi, 0)$ and $(0, \pi)$ shown in Fig.2a. Inside the TSF $h_{c1} < h < h_{c2}$, the bulk is gapped with two pairs of gapless edge states at $k_y = 0, \pi$ on the boundaries of a finite-size system in Fig.2b. Then a second topological transition from the TSF to BI at $h_{c2} = |\xi(0, 0)| = |\xi(\pi, \pi)| = 2t(\cos \alpha + \cos \beta)$ where $\Delta = 0$ and the $E_{\mathbf{k}-}$ touches zero quadratically and simultaneously at $\mathbf{k} = (0, 0)$ and $(0, \pi)$ in Fig.2c. In the BI $h > h_{c2}$, it has a bulk gap due to the Zeeman field in Fig.2d.

One can understand some qualitative features near h_{c2} in Fig.2 starting from the non-interacting SOC fermion spectrum (namely the helicity basis) with no pairing $\Delta = 0$. At $h = 0$ which is the left vertical axis in Fig.1, any $U < 0$ leads to a trivial SF. At $h_{c2} = 2t(\cos \alpha + \cos \beta)$, there is a quadratic band touching at $(0, 0)$ and (π, π) where there is already a gap $h - 2t(\cos \alpha - \cos \beta) = 4t \cos \beta$ opening at $(0, \pi)$ and $(\pi, 0)$. At $0 < h < h_{c2} = 2t(\cos \alpha + \cos \beta)$, due to the finite density of state (DOS) at the FS $\mu = 0$, a weak $U < 0$ leads to a TSF with the $p_x + ip_y$ pairing across 2 FS with the same helicity leading to $C = 2$. Here one gets a $C = 2$ TSF almost for free: at a small h and a small attractive interaction $U < 0$. At $h = h_{c2}$, the FS disappears, there is only quadratic band touching at $(0, 0)$ and (π, π) with a zero DOS, so one need a finite U_c to drive to a trivial SF. This explains why the $h = h_{c2}$ is a straight line ending at U_c at the M point in Fig.1. When $h > h_{c2}$, there is a band gap due to the Zeeman field at $\mu = 0$, so one need even a larger U_c to reach a SF. It turns out to be a 1st order transition to a trivial SF at h_b due to a jumping of the superfluid order parameter Δ , so it is a bosonic transition with gapped fermionic excitations on both sides of the transition.

If either α or β is $\frac{\pi}{2}$ (assuming $\alpha = \frac{\pi}{2}$), the two groups take the same value $\xi^2(\mathbf{k}_0) = 4t^2 \cos^2 \beta = h_c^2$ which divides the system into only 2 different phases as shown in Fig.7. The TSF phase is squeezed to zero. At $h < h_c$, it is in the trivial SF phase with a bulk gap and no edge states. At $h = h_c$, the excitation energy $E_{\mathbf{k}-}$ touches zero quadratically and simultaneously at all four points shown in the inset of Fig.7. At $h > h_c$, it gets into the gapped BI phase.

In the rest of paper, the main text focus on the isotropic Rashba limit $\alpha = \beta$ where $\xi^2(0, \pi) = \xi^2(\pi, 0) = 0$. In the anisotropic limit $\alpha \neq \beta$, h_{c1} increases, the TSF phase shrinks (Fig.6). In the extremely anisotropic limit $\alpha = \pi/2$, $h_{c1} = h_{c2} = h_c$, the TSF phase shrinks to zero and disappears (Fig.7). They will be discussed in details in the appendix.

3. The bosonic BI to SF phase transition at $h = h_b$.

The BI to the SF transition is a first order one at h_b in Fig.1. In the BI, $\Delta = 0$, the fermionic gap is due to the Zeeman field. In the SF, $\Delta \neq 0$, the fermionic gap is due to the pairing. So the transition is a bosonic one with the superfluid order parameter Δ , the fermionic excitations has gaps on both sides. The first order transition may lead to a possible " phase separation" between the SF

and BI in the two metastable regimes shown in Fig.1. Obviously, it is the SOC which leads to the multi-minima structure of the ground state energy landscape leading to the first order BI-SF transition. In fact, as shown in³², the SOC also leads to multi-minima structure of magnon spectrum in spin-orbital correlated magnetic phases. So it is a generic feature for the SOC to lead to multi-minima structures in both the ground state and the excitation spectra.

This conventional first order SF-BI transition will be contrasted to the topological first order SF-TSF transition in the next section.

4. The fermionic SF to the TSF transition at $h = h_{c1}$.

In the bulk, the transition is driven by the gap closing of the two Dirac fermions at $(0, \pi)$ and $(\pi, 0)$ with the same chirality. The mass of the Dirac fermions change signs across the TQPT. Due to the Time reversal symmetry breaking by the Zeeman field, it is a Z class, so Chern number is an integer. In the TSF in Fig.1, the Chern number $C = 2$,

1. Topological third order transition

Now we derive the effective 2×2 Hamiltonian $H(\vec{k})$ to describe the TQPT near $h = h_{c1}$. Following⁷ and projecting to the 2 component low energy spinor: $\phi_{L\mathbf{k}} = \frac{1}{\sqrt{2}} \begin{bmatrix} c_{-\mathbf{k}\uparrow}^\dagger - c_{\mathbf{k}\downarrow} \\ c_{-\mathbf{k}\downarrow}^\dagger - c_{\mathbf{k}\uparrow} \end{bmatrix}$ space, we find the effective Hamiltonian near $(0, \pi)$:

$$H_{(0,\pi)} = \left(\delta h - \frac{t^2 \cos^2 \alpha (q_x^2 - q_y^2)^2}{2\Delta} \right) \sigma_3 + 2t \sin \alpha (q_x \sigma_1 + q_y \sigma_2) \quad (2)$$

where the Dirac fermion mass $M = \delta h = h - h_{c1}$ changes the sign across the TQPT boundary $h = h_{c1}$. Note that because the SF order parameter Δ remains a constant across the TQPT, so it is just a pure fermionic TQPT inside the SF with the dynamic exponent $z = 1$.

Eq.2 can be cast into the form:

$$H(\vec{q}) = \epsilon(\vec{q}) + d_a(\vec{q})\sigma_a, \quad d_a(\vec{q}) = (Aq_x, Aq_y, M(\vec{q})) \quad (3)$$

where $\epsilon(\vec{q}) = 0$ dictated by the P-H symmetry, $A = 2t \sin \alpha$ and $M(\vec{q}) = \delta h - B(q_x^2 - q_y^2)^2$ where $B = \frac{t^2 \cos^2 \alpha}{2\Delta} > 0$.

The first Chern number is given by:

$$C_1 = \frac{1}{4\pi} \int dq_x dq_y \hat{\mathbf{d}} \cdot \left(\frac{\partial \hat{\mathbf{d}}}{\partial q_x} \times \frac{\partial \hat{\mathbf{d}}}{\partial q_y} \right) \quad (4)$$

where $\hat{\mathbf{d}}(\vec{q}) = \mathbf{d}(\vec{q})/|\mathbf{d}(\vec{q})|$ is a unit vector and the integral is over the 2d BZ in the original lattice model, but the whole 2d (k_x, k_y) plane in the continuum limit. In the TSF, $\delta h/B > 0$, $C_1 = 1$. The two Dirac fermions lead to $C = 2$. In the trivial SF, $\delta h/B < 0$, $C_1 = 0$. The mass $M = \delta h$ changes sign at the TQCP and is the only relevant term. The $-B(q_x^2 - q_y^2)^2$ term is dangerous leading

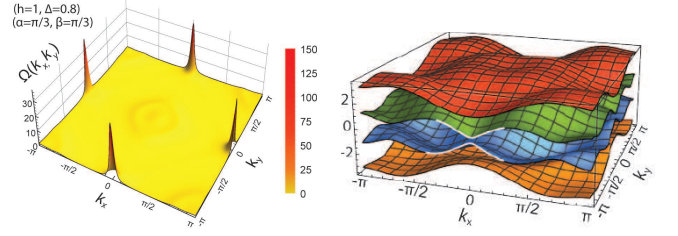


FIG. 3. (Color online) The Berry curvatures and energy bands at $[\alpha, \beta] = [\frac{\pi}{3}, \frac{\pi}{3}]$ near h_{c1} with $(h = 1, \Delta = 0.8)$ inside the TSF. (a) The Berry curvature is sharply peaked at $(0, \pi)$ and $(\pi, 0)$. (b) The four quasi-particle energy bands. The two middle bands have a minimum gap denoted by the wide lines which leads to the Berry curvature in (a) near $(0, \pi)$ and $(\pi, 0)$.

irrelevant near the TQCP in the sense that it is irrelevant at the TQCP, but it is important on the two sides of the TQCP and decide the thermal Hall conductivity of the two phases³⁹. It is important to stress that if changing $-B(q_x^2 - q_y^2)^2$ to $-B(q_x^2 - q_y^2)$, then $C_1 = 1$ would change to $C_1 = 1/2$. Incorporating the other Dirac fermion at $(\pi, 0)$, it describes a TQPT from $C = -1$ TSF to $C = 1$ TSF with the same jump of the Chern number $\Delta C = 2$ when away from half filling⁴⁰.

From Eq.2, one can determine the energy

$$E_{\pm}(\mathbf{q}) = \pm \sqrt{\delta h^2 + 4t^2 \sin^2 \alpha (q_x^2 + q_y^2)} \quad (5)$$

which has a minimum at $\mathbf{q} = (0, 0)$ as shown in Fig.3b. It will be useful to examine the bulk-edge correspondence near h_{c1} to be shown in Appendix E.

Following⁷, using the effective Hamiltonian Eq.2, one can calculate the ground state critical exponent and compare with the numerical calculations using the original 4-bands Hamiltonian Eq.A2 in the whole BZ. Following the procedures in⁷, we find the ground state energy shows a singularity at its third order derivative at the transition, so it is a 3rd order TQPT.

One can get the effective Hamiltonian at $(\pi, 0)$ by changing $\sigma_1 \rightarrow -\sigma_1, \sigma_2 \rightarrow -\sigma_2$ in Eq.2 or equivalently $A \rightarrow -A$ in Eq.3, but still with the same ϕ_L , so the pairing remains the $p_x + ip_y$ form. Then Eq.4 shows $C_{(\pi,0)} = C_{(0,\pi)} = 1$, so the total Chern number $C = C_{(\pi,0)} + C_{(0,\pi)} = 2$. Of course, $H_{(0,\pi)}$ and $H_{(\pi,0)}$ are related by the $[C_4 \times C_4]_D$ symmetry at $\alpha = \beta$. In fact, the topological Chern number of a given band is the integral of the Berry curvature in the whole BZ shown in Eq.D2. Here we show that the global topology can be evaluated just near a few isolated P-H symmetric points in an effective Hamiltonian in the continuum limit. Note that the topological Z_2 indices (Pfaffian) are also evaluated at some isolated symmetric points²⁶. They determine the topology of the bands in the whole BZ.

Using the original 4 bands theory and the three different methods outlined in the appendix D, we calculated the Berry Curvature of $E_{-}(\mathbf{q})$ in the whole BZ in Fig.3a and find that near h_{c1} , they are sharply peaked at $(0, \pi)$

and $(\pi, 0)$. The corresponding 4 energy bands are also shown in Fig.3a. These facts can be precisely captured by the 2 bands effective theory Eq.2.

2. Topological Tri-critical point and topological first order transition

Note that as shown in the last section, Eq.2 remains a third order transition until to the Topological Tri-critical (T) point in Fig.1. The h_{c1} along the short segment from the T to the M point is defined as $E(\pm\Delta_+) = E(\pm\Delta_-)$ where the energy of the two smaller minima $\pm\Delta_+$ become degenerate with that at the two larger minima $\pm\Delta_-$ shown in the top insets of Fig.1. By this definition, the h_{c1} is very close to (but not exactly the same as) the maximum value sandwiched between Δ_+ and Δ_- , namely $\Delta_+ < h_{c1} < \Delta_-$. There is a finite jump from the smaller SF order parameter $\Delta_+ < h_{c1}$ in the TSF to the larger SF order parameter $\Delta_- > h_{c1}$ in the SF across the phase boundary $h = h_{c1}$. So it becomes a Topological first order transition across which the Dirac fermion mass jump from a finite positive value $\delta h = h_{c1} - \Delta_+ > 0$ in the TSF side to a finite negative value $\delta h = h_{c1} - \Delta_- < 0$ in the SF side. So there are any mixtures of the TSF and SF at any ratios along this segment of h_{c1} . Eq.2-Eq.5 remain valid with $\Delta = \Delta_+$ in the TSF side and $\Delta = \Delta_-$ in the SF side respectively.

In sharp contrast to the first order BI-SF transition discussed in last section, there is no change of symmetries across this topological first order SF-TSF transition. The Chern number just jump from 0 to 2. Of course, there is no gap closing across both first order transitions. In fact, there is not a single example a topological transition is found to be second order. Although there is no exact proof on this fact yet, we conjecture that any topological transition must be odd order.

5. The bosonic/fermionic TSF to the BI transition at $h = h_{c2}$.

Near $h_{c2} = 2t(\cos \alpha + \cos \beta)$, there are quadratic band touching at $(0, 0)$ and (π, π) as shown in Fig.2c. Following similar procedures as those to derive the 2×2 effective Hamiltonian Eq.2 near h_{c1} and $(0, \pi)$, we derive the 2×2 effective Hamiltonian near h_{c2} and $(0, 0)$:

$$H_{(0,0)} = \left(\delta h - t \frac{1 + \cos^2 \alpha}{2 \cos \alpha} (q_x^2 + q_y^2) \right) \sigma_3 - \frac{\Delta \tan \alpha}{2} (q_x \sigma_1 + q_y \sigma_2) \quad (6)$$

where the two component low energy spinor $\phi_{L\mathbf{k}} = \frac{1}{\sqrt{2}} \begin{bmatrix} c_{-\mathbf{k}\downarrow}^\dagger \\ c_{\mathbf{k}\downarrow} \end{bmatrix}$ which contains only spin down. The Dirac fermion mass $M = \delta h = h_{c2} - h$ changes its sign across the TQPT boundary $h = h_{c2}$. In the BI side $\delta h < 0, \Delta = 0$, it becomes a gapped non-relativistic fermion due to the Zeeman field: $E(k) \sim [h - h_{c2}] + B(q_x^2 + q_y^2)$. In the TSF side $\delta h > 0, \Delta \neq 0$, there is also a gap opening due to the effective $p_x + ip_y$ pairing Δ , it describes the TSF with $C = 2$. It has the dynamic exponent $z = 2$ at the QCP $\delta h = 0, \Delta = 0$.

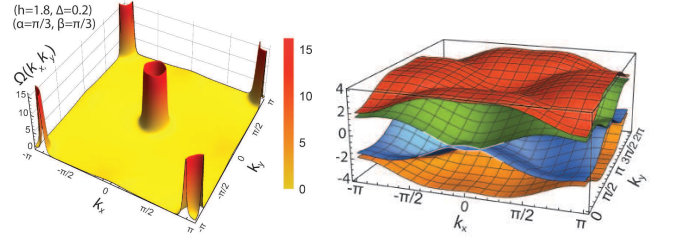


FIG. 4. (Color online) The Berry curvatures and energy bands at $[\alpha, \beta] = [\frac{\pi}{3}, \frac{\pi}{3}]$ near h_{c2} with $(h = 1.8, \Delta = 0.2)$ inside the TSF. (a) The Berry curvature has a dip at $(0, 0)$ and (π, π) , but peaked at a ring around the two Dirac points. (b) The four quasi-particle bands. The two middle bands have the shape denoted by the wide lines near $(0, 0)$ and (π, π) . The energy gap contour of the two middle bands (not shown here, but see Fig.8) are nearly circular which leads to the Berry curvature structure in (a). This bulk feature leads to the oscillating behavior of the edge state wavefunction when decaying into the bulk shown in appendix E.

Eq.6 can also be cast into the form Eq.3 where $\epsilon(\vec{k}) = 0$, $A = \frac{\Delta \tan \alpha}{2}$ and $M(\vec{k}) = \delta h - B(q_x^2 + q_y^2)$, $B > 0$. The first Chern number is still given by Eq.4: If $M/B > 0$ and $\Delta \neq 0$ in the TSF, $C_1 = 1$. If $M/B < 0$ and $\Delta = 0$ in the BI, $C_1 = 0$. So there are two relevant operators: the mass term $M = \delta h$ and the $p_x + ip_y$ pairing term Δ . The $-B(q_x^2 + q_y^2)$ term is dangerous leading irrelevant near the QCP in the sense that it is irrelevant at the QCP, but it is important to the physical properties of the two phases on the two sides of the QCP.

One can determine the bulk energy spectrum:

$$E_{\pm}(\mathbf{q}) = \pm \sqrt{[M - B(q_x^2 + q_y^2)]^2 + A^2(q_x^2 + q_y^2)} \quad (7)$$

which means that in the TSF side $M = \delta h > 0$, if assuming $C = 2MB - A^2 > 0$, then it has a maximum at $\mathbf{q} = (0, 0)$ and a minimum at $q^2 = C/2B^2$ with a minimum gap $E_{min} = \frac{A\sqrt{4MB - A^2}}{2B} > 0$. This is indeed the case as shown in Fig.4b. This structure of the bulk gap is crucial to explore the bulk-edge correspondence near h_{c2} in the appendix E.

The main difference between the TQPT at $h = h_{c1}$ described by Eq.2 and that at h_{c2} described by Eq.6 is that in the former, the SF order parameter Δ is non-critical across the SF to TSF transition at h_{c1} , the effective $p_x + ip_y$ pairing amplitude in Eq.2 is given by the SOC strength $t \cos \alpha$, so it is a pure fermionic transition. However, in the latter, the SF order parameter Δ is also critical across the TSF to the BI transition at h_{c2} , the effective $p_x + ip_y$ pairing amplitude in Eq.2 is given by the S-wave pairing Δ multiplied by an SOC related factor $\tan \alpha$. So it involves two natures instead of just a pure fermionic transition: (1) Conventional bosonic nature due to the superfluid order parameter Δ . (2) Topological fermionic nature due to the Dirac fermions in the TSF side. It happens near the two Dirac points $(0, \pi)$ and $(\pi, 0)$ near h_{c1} in the Fig.1. However, it moves to $(0, 0)$

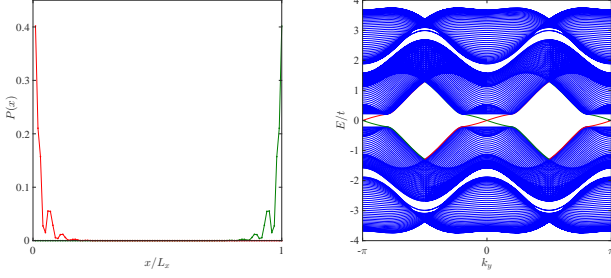


FIG. 5. (Color online) The normalized edge state wavefunction of the TSF in both real and momentum space at the two edges $x = 0, L$ and at $k_y = 0$. The SOC parameters are $[\alpha, \beta] = [\frac{\pi}{3}, \frac{\pi}{3}]$ and the (h, Δ) corresponding to one point inside the TSF labeled in Fig.2. (a) In the real space, it shows some oscillating behaviors towards decaying into the bulk. The red and green lines show the two oppositely propagating edge modes on the two opposite sides of the sample. (b) In the momentum space, it shows two edge states at $k_y = 0, \pi$. The red and green lines correspond to those in (a).

and (π, π) near h_{c2} . From the 2×2 effective Hamiltonian Eq.6, one may construct a Ginsburg Landau theory with the critical SF order parameter Φ in the bosonic sector couples to the critical fermionic excitations in the fermionic sector.

One can get the effective Hamiltonian at (π, π) by changing $\sigma_1 \rightarrow -\sigma_1, \sigma_2 \rightarrow -\sigma_2$ in Eq.6 or equivalently $A \rightarrow -A$ in Eq.3. Especially, it has a different low energy two component spinor $\phi_{L\mathbf{k}} = \frac{1}{\sqrt{2}} \begin{bmatrix} c_{\mathbf{k}\uparrow} \\ c_{-\mathbf{k}\uparrow}^\dagger \end{bmatrix}$ which contains only spin up. Then Eq.4 shows $C_{(\pi, \pi)} = C_{(0,0)} = 1$, so the total Chern number $C = C_{(\pi, \pi)} + C_{(0,0)} = 2$ in the TSF. So the distribution of the Berry curvature is moving from $(0, \pi)$ and $(\pi, 0)$ near h_{c1} as shown in Fig.3a to $(0, 0)$ and (π, π) near h_{c2} shown in Fig.4a. Indeed, using the original 4 bands theory, using three different methods outlined in the appendix D, we calculated the Berry Curvature of $E_-(\mathbf{q})$ in the whole BZ in Fig.4a and find they are localized around $(0, 0)$ and (π, π) near h_{c2} shown in Fig.4a. The corresponding 4 energy bands are also shown in Fig.4b. These facts can be precisely captured by the 2 bands effective theory Eq.6.

6. Edge modes in the TSF

As shown in Fig.2,5, using the open boundary conditions in the x directions, in the TSF near h_{c1} , the Exact Diagonalization (ED) study shows that there are two branches of Majorana fermion edge states $k_y = 0$ and $k_y = \pi$. In the trivial SF side, $C = 0$ with no edge states. In the following, we analyze the two edge modes from the effective actions Eq.2 near h_{c1} and Eq.6 near h_{c2} respectively.

1. Edge states near h_{c1} .

As shown in Eq.2, the effective $p_x + ip_y$ pairing amplitude $\Delta_e = 2t \sin \alpha$ is relatively large, so the TSF has a relatively large gap. As shown in appendix E, setting $q_x \rightarrow -i\partial_x$ at any given q_y in the 2×2 effective Hamiltonian

Eq.2 around $(0, \pi)$ or $(\pi, 0)$, one can determine the edge state γ_2 near $k_y = \pi$ in Eq.E6 and γ_1 near $k_y = 0$ respectively. One can write the effective 1d Majorana fermion $\gamma_i^\dagger = \gamma_i, i = 1, 2$ edge Hamiltonian:

$$H_{edge} = \int dy [-iv_f \gamma_i \partial_y \gamma_i] \quad (8)$$

where $i = 1, 2$ stand for the two edge modes and $v_f = \Delta_e = 2t \sin \alpha$ is the edge velocity near h_{c1} .

The original edge Majorana fermion on the edge $x = 0$ can be expressed in terms of the two edge modes:

$$\psi_1(y) = \gamma_1(y) + (-1)^y \gamma_2(y) \quad (9)$$

where $\psi_1^\dagger(y) = \psi_1(y)$. So one can evaluate the Majorana fermion correlation functions along the 1d $x = 0$ edge Eq.8 and 9.

Fig.5a shows the wavefunction of the edge mode at a given k_y which was achieved by ED a $4L_x \times 4L_x$ matrix at any given k_y . Notably, the edge state wavefunction at a given k_y decay into the bulk with some oscillating behaviors. As shown in Appendix E, the edge eigenvalue could have both real and imaginary part, the real part leads to decay length into the bulk, while the imaginary part leads to the oscillations which are indeed observed in the ED results in Fig.5.

In fact, one can define another Majorana edge mode $\psi_2(y) = \gamma_1(y) + (-1)^{y+1} \gamma_2(y)$ which is decoupled, so plays no role. It is easy to check that for the two sets of Majorana fermions³⁶: $\{\gamma_i(y), \gamma_j(y')\} = \delta_{ij} \delta(y - y'), \gamma_i^\dagger(y) = \gamma_i(y), \psi_i^\dagger(y) = \psi_i(y), \{\psi_i(y), \psi_j(y')\} = 2\delta_{ij} \delta(y - y'), i, j = 1, 2$. The extra factor of 2 shows that the edge state contains 2 Majorana fermions.

2. Edge states near h_{c2} .

As shown in Eq.6, the effective $p_x + ip_y$ pairing amplitude $\Delta_e = \Delta \tan \alpha / 2$ is relatively small, so the TSF has a relatively small gap. One can use the effective action Eq.6 to derive the edge modes in the continuum limit. It was first studied in³⁵ by ignoring the quadratic $-B(q_x^2 + q_y^2)$ term. When taking this quadratic term into account, it was computed in Ref.⁴ in the context of quantum anomalous Hall effects (QAH). The main difference is that Ref.⁴ is for QAH, so the edge is the 1d helical edge state, Here it is a Majorana fermion edge state dictated by the PH symmetry.

In the appendix E, we get the edge mode γ_3 near $k_y = 0$ in Eq.E11 and γ_4 near $k_y = \pi$ in Eq.E13. So we reach the same Eq.9 with $v_f = \Delta_e = \Delta \tan \alpha / 2, i = 3, 4$ and $\psi_3(y) = \gamma_3(y) + (-1)^y \gamma_4(y)$. The crucial differences than the two Majorana fermions γ_1, γ_2 near h_{c1} is that γ_3 and γ_4 near h_{c2} contain only spin down and spin up respectively. Their wavefunctions may also different spatial dependencies as shown in Eq.E3 and Eq.E9.

When moving from h_{c1} to h_{c2} inside the TSF, we expect the edge mode will crossover from the equal spin superposition in γ_1 to just spin down in γ_3 near $k_y = 0$, the equal spin superposition in γ_2 to just spin down in γ_4 near $k_y = \pi$. Of course, the two edge modes stay near

$k_y = 0$ and $k_y = \pi$ as dictated by the symmetries of the Hamiltonian.

7. Majorana bound states inside a vortex core of the TSF

It was known that at a $C = 1$ TSF, a $n = \pm 1$ vortex holds one Majorana fermion zero mode^{3,4}. Here, we have a $C = 2$ TSF in Fig.2 with two chiral edge modes. In general, it is expected that the Chern number $C = 2$ is equal to the number of edge modes and also the number of Majorana zero modes inside a $n = \pm 1$ vortex core. Similar to the study of the edge states, one can use the effective action near h_{c1} and h_{c2} to study analytically the zero modes inside a S-wave vortex core. When introducing a vortex in the phase winding of the SF order parameter, it will affect most the low energy fermionic responses near $(0, \pi)$ and $(\pi, 0)$ when h is near h_{c1} or near $(0, 0)$ and (π, π) when h is near h_{c2} respectively. The existence and stability of the zero modes are protected by the Chern number Z class classification of the TSF, so are independent of the continuum approximation made in the effective actions. Similar continuum approximations were used to study the quasi-particles in the vortex states of high T_c superconductors³⁹.

1. Majorana zero modes near h_{c1}

In the 2×2 effective Hamiltonian Eq.2 near $(0, \pi)$ with $C = 1$, setting $\Delta \rightarrow \Delta_0 e^{i\theta}$, the first term remains intact, but the SOC strength in the second term $t \sin \alpha \rightarrow t \sin \alpha e^{i\theta}$ acquires an effective phase from the order parameter phase winding. Setting $q_x \rightarrow -i\partial_x$, $q_y \rightarrow -i\partial_y$ and paying special attentions to the anisotropy in the $-B(q_x^2 - q_y^2)^2$ term, one may derive the wavefunctions $(u(\mathbf{r}), v(\mathbf{r}))$ satisfying $u^*(\mathbf{r}) = -v(\mathbf{r})$. It leads to the Majorana fermion γ_2 in Eq.F2 which contains both spin up and spin down. One can do a similar calculation near $(\pi, 0)$ to get the second trapped Majorana zero mode γ_1 which also contains both spin up and spin down. One may combine the two trapped Majorana zero modes inside a S-wave vortex core near h_{c1} into a single Dirac fermion:

$$\psi_1 = \gamma_1 + i\gamma_2 \quad (10)$$

Its number $\psi_1^\dagger \psi_1 = 0, 1$ counts the occupations on the zero mode. Its exchange statistics is just a fermionic one. There is no long-range entanglement between two distant vortices. A local operation can change the Dirac fermion occupation number inside the vortex core²⁷.

2. Majorana zero modes near h_{c2}

Similarly, in the 2×2 effective Hamiltonian Eq.6 near $(0, 0)$ with $C = 1$, setting $\Delta \rightarrow \Delta_0 e^{i\theta}$, the first term remains intact, the second term $\Delta \tan \alpha \rightarrow \Delta_0 \tan \alpha e^{i\theta}$ acquires the phase and is nothing but a $p_x + ip_y$ pairing vortex. The Majorana fermion zero mode inside such a cylindrical symmetric vortex core in the polar coordinate (r, θ) has been worked out in many previous literatures^{8,9,35}. One get the Majorana fermion γ_3 in Eq.F4 which contains only spin down. One can also get the other Majorana fermion zero mode γ_4 in Eq.F6 which contains only spin up. Combining the two trapped Majorana zero

modes inside a S-wave vortex core near h_{c2} leads to a single Dirac fermion $\psi_2 = \gamma_3 + i\gamma_4$.

It is instructive to compare Eq.9 with Eq.10 which leads to the following interesting edge-vortex core correspondence. In the former, the two Majorana edge modes are separated by the conserved momentum $k_y = \pi$ along the $x = 0$ edge, so their linear combination leads to the Majorana fermion ψ_1 with a twice magnitude. While, in the latter, the two Majorana edge modes are trapped inside the same vortex core, so can be combined into one Dirac fermion. Interesting edge-vortex core correspondences in terms of spin structure are explored further in Appendix F.

8. Experimental searching for the TSF

It was known that the phases and phase transitions in a lattice are different and much richer than those in a continuum. However, so far, there are very few theoretical works on a optical lattice⁸. The goal of this work is to predict the regime in (h, U) and N to search for topological superfluids and the topological transitions to its neighboring quantum phases, study the properties of the TSF, the nature of these transitions and their experimental detections. In fact, in cold atom experiments, the chemical potential μ is not measurable or controllable, only the number of atoms N is, so the self-consistence equations must be imposed to get the realistic phases and phase transitions in (h, U) at a given N and to have any experimental impacts. In the present system, the BI only happens in a lattice. So the TSF to BI transition at h_{c2} in Fig.1 and Fig.2 only happens in a lattice. The TSF happens in the small h and small U in the Fig.1 which is the experimentally most easily accessible regimes. This fact is also very crucial for all the current experiments¹²⁻¹⁶ to probe possible many body effects of SOC fermion or spinor boson gases, because so far, the heating effects are controllable only at weak couplings, which get more problematic as the interaction gets stronger.

The topological order of the TSF does not survive up to any finite T . Of course, the BI does not survive up to any finite T either. There should be a KT transition above both the SF and TSF. The T_{KT} can be estimated as $T_{KT} \sim t \sim 3nK$ which is clearly experimental reachable with the current cooling techniques^{18,19}. Using Eq.2 and following the procedures in⁷, one may also write down the finite temperature scaling functions for several physical quantities such as specific heats, compressibility, Wilson ratio and thermal Hall conductivity³⁹ across the $T = 0$ SF to the TSF transition near h_{c1} in Fig.1. Following the quantum impurity problems³⁷, one may also calculate the leading corrections to the scalings due to the leading dangerously irrelevant $-B(q_x^2 - q_y^2)^2$ operator.

Now we discuss the experimental detections of Fig.1-8. All the phases, bulk excitations, edge modes and phase transitions shown in Fig.1-8 are at $T = 0$. But they are responsible for all the experimental measurable quantities at a finite temperature⁷. The fermionic quasi-particle spectrum can be detected by photoemission spectroscopy²⁰. The topological phase transitions and

the BCS to BEC crossovers in Fig.1,6,7 can also be monitored by the radio-frequency dissociation spectra^{21,28}. The energy gaps of the two middle bands in Fig.3b and Fig.4b can be detected by the momentum resolved interband transitions²². The bulk Chern numbers can be measured by the techniques developed in²³. The edge states can be directly imaged through Time of flight kind of measurements²⁴. A vortex can be generated by rotating the harmonic trap⁴⁷. The Majorana zero modes and the associated spin structures inside the vortex core can be imaged through In Situ measurements²⁵.

9. Conclusions and discussions It is constructive to compare the $C = 2$ TSF with the 2d Time Reversal invariant TSF which is one copy of 2d $p_x + ip_y$ TSF with spin up plus its Time reversal partner of a 2d $p_x - ip_y$ with spin down⁴. In fact, after a unitary transformation, the surface of a 3d Topological insulator in the proximity of a S-wave superconductor also belongs to the same class of 2d Time-reversal invariant TSF³. Its two edge modes carry opposite spin and flow in opposite (chiral) direction. It is characterized by the Z_2 topological invariant. Here, the $C = 2$ TSF has also two copies of 2d $p_x + ip_y$ TSF related by the $\mu = 0$ symmetry. However, the two edge modes are separated by the momentum $k_y = \pi$, flow in the same (chiral) direction. It is characterized by the Z topological invariant. As shown in the appendix E, the two edge modes carry the same spin structure near h_{c1} , but opposite spin near h_{c2} . There were previous studies on nearly zero modes inside a vortex core of a superconducting state in graphene³⁸. There are four of them. However, these four zero modes appear only in linear approximation, but are not protected by any topological indices, therefore can be lifted by lattice effects, in sharp contrast to the $C = 2$ Majorana zero modes here which are protected by the Z class of TSF.

The multi-minima structure in the ground states in Fig.1 is responsible to the 1st order transition between the BI and the SF, also the topological first order transition between the SF and the TSF. First order transitions also happen between Y-x state and an In-commensurate phase in the Rotated Heisenberg model in the generic (α, β) phase diagram⁵⁴. These first order transitions lead to associated phase separations, meta-stable phases and hysteresis. In fact, the multi-minima structure also exists in the excitations above a commensurate ground state³². All these salient features are due to SOC.

Fig.1 and Fig.2 show that both the TSF and trivial SF are fully gapped, there is no fermions left unpaired. This is another salient feature due to the SOC which favors SF phase in a Zeeman field. It is the SOC which splits the FS leading to complete pairings even in a Zeeman field. This is in sharp contrast to S-wave pairing of spin-imbalanced fermions without SOC due to a Zeeman field where there are always fermions left unpaired⁴⁶. The absence of FFLO state of a SOC fermions in a Zeeman field in a negative interaction reflects well the absence of Ferromagnetic state in a SOC fermions in a repulsive interaction^{53,55}. All these phenomena are another salient

feature due to SOC.

The paper is at the BCS mean field level. It maybe important to incorporate the quantum fluctuation effects. By writing the pairing $\Delta = \sqrt{\Delta_0 + \delta\rho}e^{i\theta}$, at the half filling $\mu = 0$, we expect there exists both gapless Goldstone mode θ and stable gapped Higgs mode $\delta\rho$ as the collective excitation⁴⁸ inside both the TSF and trivial SF. Near h_{c1} in Eq.2, it is important to study the coupling between the Goldstone mode, also the Higgs mode and the gapless Dirac fermions at $(0, \pi)$ and $(\pi, 0)$ to investigate how the gapless Goldstone mode changes the universality class of the TQPT at h_{c1} , also the decay rate of the Higgs mode. Near h_{c2} in Eq.6, following the methods developed in^{39,51}, it is interesting to construct a Ginsburg Landau action to perform a Renormalization group analysis. This action will include the bosonic sector for the superfluid order parameter $\Phi(\mathbf{r})$, the fermionic sector $\psi(\mathbf{r})$ at $(0, 0)$ and (π, π) for the topological order and an effective $p_x + ip_y$ coupling between the two sectors. Between h_{c1} and h_{c2} , the $C = 2$ TSF has a fermionic gap in the bulk, but two gapless modes Eq.8, it maybe interesting to study how the bulk gapless Goldstone mode interacts with the two edge modes.

Going beyond the half-filling, then the chemical potential μ need to be determined self-consistently. The $\mu = 0$ symmetry is lost. For general μ , α, β , the four $\xi_{\mathbf{k}_0}^2$ in Eq.A7 could take four different values, so when tuning the Zeeman field through $h = \sqrt{\xi_{\mathbf{k}_0}^2 + \Delta^2}$ in Eq.A7, one may drive the system to undergo four transitions into five phases, especially $C = \pm 1$ TSF. It will be discussed in a separate publication.

We thank W. M. Liu for encouragements and acknowledge AFOSR FA9550-16-1-0412 for supports.

Supplementary Materials for "Searching new topological superfluids and phase transitions with spin-orbit coupled fermions in an optical lattice".

Appendix A: Mean field calculations and self-consistent equations

By introducing the pairing order parameter Δ , one can rewrite the on-site interacting term in Eq.1 as:

$$H_\Delta = -\Delta \sum_i \left(c_{i\uparrow}^\dagger c_{i\downarrow}^\dagger + c_{i\downarrow} c_{i\uparrow} \right) - \frac{L_x L_y}{U} \Delta^2 \quad (\text{A1})$$

where the order parameter Δ should be determined by minimizing the free energy of the system.

For a uniform Δ , it is convenient to transform the operator from the real space into the momentum space: $c_i = \frac{1}{\sqrt{L_x L_y}} \sum_{\mathbf{k}} e^{i\mathbf{k} \cdot \mathbf{i}} c_{\mathbf{k}}$ where $\mathbf{k} = [\frac{\pi n_x}{L_x}, \frac{\pi n_y}{L_y}]$ with $n_{x/y} = -L_{x/y}, -L_{x/y} + 1, \dots, L_{x/y}$, which becomes continuous in the thermodynamic limit $L_{x/y} \rightarrow \infty$.

Finally, we can rewrite the mean-field Hamiltonian in

the Nambu representation:

$$H_{MF} = \sum_{\mathbf{k}} \left(\frac{1}{2} \begin{bmatrix} c_{\mathbf{k}\uparrow}^\dagger & c_{\mathbf{k}\downarrow}^\dagger & c_{-\mathbf{k}\uparrow} & c_{-\mathbf{k}\downarrow} \end{bmatrix} \begin{bmatrix} \xi_{\mathbf{k}} - h & \Lambda_{\mathbf{k}} & 0 & -\Delta \\ \Lambda_{\mathbf{k}}^\dagger & \xi_{\mathbf{k}} + h & \Delta & 0 \\ 0 & \Delta & -\xi_{\mathbf{k}} + h & \Lambda_{\mathbf{k}}^\dagger \\ -\Delta & 0 & \Lambda_{\mathbf{k}} & -\xi_{\mathbf{k}} - h \end{bmatrix} \begin{bmatrix} c_{\mathbf{k}\uparrow} \\ c_{\mathbf{k}\downarrow} \\ c_{-\mathbf{k}\uparrow}^\dagger \\ c_{-\mathbf{k}\downarrow}^\dagger \end{bmatrix} + \xi_{\mathbf{k}} \right) - \frac{L_x L_y}{U} \Delta^2 \quad (\text{A2})$$

which can be diagonalized by introducing two Bogoliubov quasi-particles $\alpha_{\mathbf{k}\pm}$:

$$H_{MF} = \sum_{\mathbf{k}} \left[E_{\mathbf{k}+} \alpha_{\mathbf{k}+}^\dagger \alpha_{\mathbf{k}+} + E_{\mathbf{k}-} \alpha_{\mathbf{k}-}^\dagger \alpha_{\mathbf{k}-} \right] + E_G \quad (\text{A3})$$

with the quasi-particle excitation energies:

$$E_{\mathbf{k}\pm} = \sqrt{\xi_{\mathbf{k}}^2 + |\Lambda_{\mathbf{k}}|^2 + h^2 + \Delta^2 \pm 2\sqrt{\xi_{\mathbf{k}}^2 [|\Lambda_{\mathbf{k}}|^2 + h^2] + h^2 \Delta^2}} \quad (\text{A4})$$

where $\xi_{\mathbf{k}} = -2t(\cos \alpha \cos k_x + \cos \beta \cos k_y) - \mu$, $\Lambda_{\mathbf{k}} = 2t(\sin \alpha \sin k_x - i \sin \beta \sin k_y)$ and the ground state energy is:

$$E_G = \sum_{\mathbf{k}} \left[\xi_{\mathbf{k}} - \frac{E_{\mathbf{k}+} + E_{\mathbf{k}-}}{2} \right] - \frac{L_x L_y}{U} \Delta^2 \quad (\text{A5})$$

At zero temperature, given the experimentally controlled parameters U, h and N , one can determine the two quantities Δ, μ by solving the self-consistent equations⁵²:

$$\begin{aligned} -\frac{\partial E_G}{\partial \mu} &= N \\ \frac{\partial E_G}{\partial \Delta} &= 0 \end{aligned} \quad (\text{A6})$$

It was shown in Sec.II that the lower branch $E_{\mathbf{k}-}$ in Eq.A4 always has four extreme points at $(k_{0x}, k_{0y}) = (0, 0), (\pi, 0), (0, \pi)$, and (π, π) . If there exists any gapless fermionic excitation (i.e. $E_{\mathbf{k}-} = 0$), it must occur at one or several of the four $\mathbf{k} = \mathbf{k}_0$ where the Eq. A4 simplifies to:

$$E_{\mathbf{k}_0-} = \left| \sqrt{\xi_{\mathbf{k}_0}^2 + \Delta^2} - h \right| \quad (\text{A7})$$

which determines the possible TQPT driven the gap closing of the fermionic excitations.

Now we focus on the half filling case. Using the $\mu = 0$ symmetries of the $E_{\mathbf{k}\pm}$ in Eq.A4, one can show that at the half-filling $N = L_x L_y$ (or $\nu = \frac{1}{2}$), the chemical potential $\mu = 0$ for any Δ . So one only need to focus on the second self-consistent Equation in Eq.A6 to determine the Δ . This substantially simplifies the determination of the ground state and phase transitions shown in the Fig.1. It turns out that the SOC leads to highly non-trivial multi-minima landscapes in the (U, h) space shown in the Fig.1. Eq.A7's implications on topological

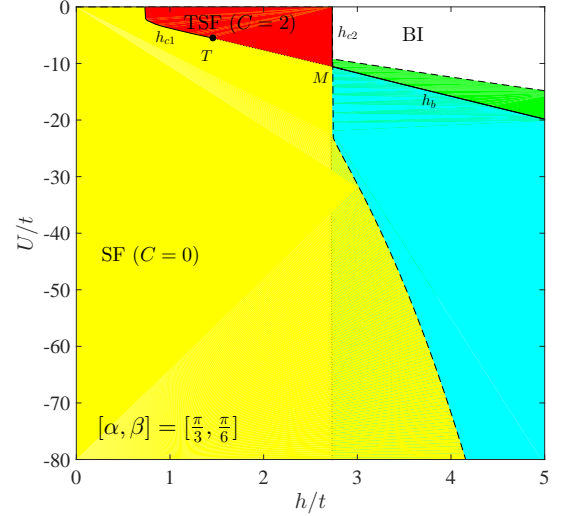


FIG. 6. (Color online) The global phase diagram in the parameter space of U and h at $[\alpha, \beta] = [\frac{\pi}{3}, \frac{\pi}{6}]$. The TSF regime starts to shrink and the h_{c1} starts to approach to h_{c2} . Compare to Fig.1.

fermionic transitions at h_{c1} and h_{c2} are presented in the main text.

The bosonic transition from the BI to the SF where the fermionic excitations are always gapped are presented in Sec.III.

Appendix B: Most general case with $\alpha \neq \beta$

The 2d SOC parameter (α, β) are experimentally tunable. When moving away from the isotropic limit $\beta < \alpha$, the $[C_4 \times C_4]_D$ symmetry is absent, the h_{c1} increases to:

$$h_{c1} = \sqrt{h_0^2 + \Delta^2} \quad (\text{B1})$$

where $h_0^2 = \xi^2(0, \pi) = \xi^2(\pi, 0) = 4t^2(\cos \alpha - \cos \beta)^2$. It vanishes in the isotropic limit $\alpha = \beta$ as discussed in the main text. While $h_{c2} = 2t(\cos \alpha + \cos \beta)$.

The phase diagram for $(\alpha = \pi/3, \beta = \pi/6)$ is shown in Fig.6 where the TSF phase regime shrinks.

Following the same procedures as those at $\alpha = \beta$, one can derive an effective action near h_{c1} and near the momentum $(0, \pi)$ or $(\pi, 0)$. However, due to the lack of the

$[C_4 \times C_4]_D$ symmetry at any $\alpha \neq \beta$, the effective action looks more complicated than Eq.2, but it is in the same universality class with a different local distribution of the Berry curvature than in Fig.3a. Similar statements can be made on the effective action near h_{c2} and near the momentum $(0,0)$ or (π,π) .

Note that despite the lack of $[C_4 \times C_4]_D$ symmetry at any $\alpha \neq \beta$, the $\mu = 0$ symmetries remain which indicate the equivalence between the effective action at $(0,\pi)$ and that at $(\pi,0)$, between the effective action at $(0,0)$ and that at (π,π) after suitable unitary transformations. Specific calculations showed that this is indeed the case.

Appendix C: The extremely anisotropic limit at $(\alpha = \pi/2, \beta)$.

It was found that in the absence of the Zeeman field, there is a spin-orbital coupled $U(1)_{soc}$ symmetry³¹ along the anisotropic limit at $(\alpha = \pi/2, \beta)$. The $U(1)_{soc}$ symmetry is kept when the Zeeman field is along the \hat{y} axis³⁴. However, it was broken when the Zeeman field is along the \hat{x} axis or the \hat{z} axis³². Similarly, the Zeeman field along the \hat{z} axis in Eq.1 also breaks the $U(1)_{soc}$. However, as said in Sec.II, the symmetry $\alpha \rightarrow \pi - \alpha, k_x \rightarrow \pi - k_x$ indicates the equivalence between $(0,0)$ and $(\pi,0)$, also between $(0,\pi)$ and (π,π) at $\alpha = \pi/2$. Then the two critical fields become the same $h_{c1} = h_{c2} = h_c = 2t \cos \beta$. The global phase diagram is shown in Fig.7 where there are only two phases SF and NI, the TSF phase is squeezed out.

The quasi-particle energy at the four points $(0,0)$, (π,π) and $(0,\pi)$, $(\pi,0)$ all touch zero quadratically at the same time. Following the similar procedures to derive Eq.2 and Eq.6, we reach the effective actions near the 4 points:

$$H_{h_c} = \pm \left[\delta h + \frac{\Delta^2}{4t \cos \beta} - \frac{t}{\cos \beta} (q_x^2 + q_y^2) \right] \sigma_3 \pm \frac{\Delta}{\cos \beta} (q_x \sigma_1 + \sin \beta q_y \sigma_2) \quad (C1)$$

where $\delta h = h_c - h$ and $(+,-)$, $(+,+)$ and $(-,+)$, $(-,-)$ are for $(0,0)$, (π,π) and $(0,\pi)$, $(\pi,0)$ respectively. When $\delta h > 0$ and $\Delta \neq 0$, it is in the SF phase. When $\delta h < 0$ and $\Delta = 0$, it is in the BI phase.

In the SF side, $\delta h > 0$ and $\Delta \neq 0$, Eq.C1 near any of the four points can also be cast into the form Eq.3 where $\epsilon(\vec{k}) = 0$ and $M(\vec{k}) = M - B(q_x^2 + q_y^2)$, $M = \delta h + \frac{\Delta^2}{4t \cos \beta}$, $B > 0$. The first Chern number is still given by Eq.4: If $M/B > 0$ and $\Delta \neq 0$ in the SF, $C_1 = \pm 1$. If $M/B < 0$ and $\Delta = 0$ in the BI, $C_1 = 0$. However, the two gapped Dirac fermions at $(0,\pi)$, $(\pi,0)$ carry the same topological charges³³ $\mu = 1$, so leading to the Chern number $C_{\mu=1} = C_{(0,\pi)} + C_{(\pi,0)} = 2$. While the two gapped Dirac fermions at $(0,0)$, (π,π) carry opposite topological charges³³ $\mu = -1$, so leading to the Chern number

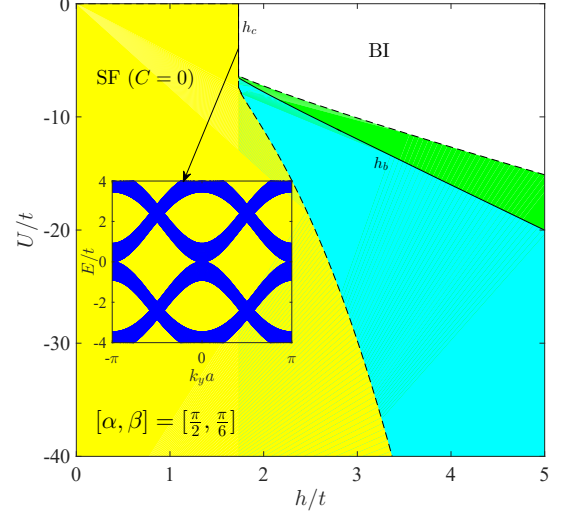


FIG. 7. (Color online) The global phase diagram in the parameter space of U and h at $[\alpha, \beta] = [\frac{\pi}{2}, \frac{\pi}{6}]$. The TSF regime shrinks to zero due to $h_{c1} = h_{c2} = h_c$. Inset: the quadratic band touching at the 4 Dirac points.

$C_{\mu=-1} = C_{(0,0)} + C_{(\pi,\pi)} = -2$. So the total Chern number is $C = 2 - 2 = 0$, it is a trivial SF. It indicates the 4 gapped Dirac fermions can annihilate without going through a phase transition.

In fact, as stressed in Sec.IV and V, the topological Chern number of a given band is the integral of the Berry curvature in the whole BZ shown in Eq.D2. Here we show that the global topology can be evaluated just near a few isolated points in an effective Hamiltonian in a continuum limit. If looking at the 4 points separately, it seems there is topological transition from a BI to a TSF with $C = \pm 1$. However, the total Chern number $C = 1 + 1 - 1 - 1 = 0$, so globally it is still a BI to a trivial SF transition shown in Fig.7.

Using the original 4 bands theory, using three different methods outlined in the appendix D, we calculated the Berry Curvature of $E_-(\mathbf{q})$ in the whole BZ in Fig.8a and find they are localized around $(0,0)$, (π,π) and $(0,\pi)$, $(\pi,0)$ respectively with $C = 1, 1, -1, -1$. The corresponding 4 energy bands are also calculated (but not shown). We only draw the energy gap contour of the two middle bands $E_{\mathbf{k}-}$ in Fig.8b which leads to the non-trivial Berry curvature structure shown in Fig.8a. All these facts can be precisely captured by the 2 bands effective theory Eq.C1.

Appendix D: The bulk Chern number calculations in both the original 4 bands and the effective 2 band theories

We solve the eigenvalue problem (numerically) $H_k |\psi_{nk}\rangle = \omega_n |\psi_{nk}\rangle$ where the H_k is given in Eq.A2

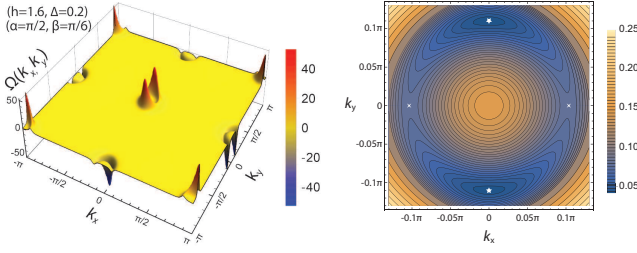


FIG. 8. (Color online) The Berry curvatures and energy bands at $[\alpha, \beta] = [\frac{\pi}{2}, \frac{\pi}{6}]$ near h_c with $(h = 1, \Delta = 0.8)$ inside the SF. (a) The Berry curvature has two split peaks along k_y axis around $(0, 0), (\pi, \pi)$ with local $C = 1$ and $(0, \pi), (\pi, 0)$ with local $C = -1$. Despite the local non-vanishing Chern numbers, the total $C = 0$. (b) The energy gap contour of the two middle bands E_{k-} have two minima denoted by two stars along the k_y axis and two saddle points denoted by the two crosses along the k_x axis. This gap structure leads to that of the Berry curvature in (a).

and the eigen-energies $\omega_1 = -E_{k+}, \omega_2 = -E_{k-}, \omega_3 = E_{k-}, \omega_4 = E_{k+}$. In the following, we use 3 different methods to calculate the Berry curvature in the original 4 bands on the square lattice. The results are shown in Fig.3, 4 and 8

1. *Method 1:* The Berry curvature for a given band is

$$\Omega_n(k) = i[(\partial_x \psi_{nk}^*)(\partial_y \psi_{nk}) - (\partial_y \psi_{nk}^*)(\partial_x \psi_{nk})] \quad (D1)$$

We numerically evaluate the Chern number by an integration over the whole BZ:

$$C_n = \frac{1}{2\pi} \int_{\text{BZ}} d^2k \Omega_n(k) \quad (D2)$$

Using the default numerical integration method, we obtained $C_2 = 1.9999999887582889 = 2$ when $[\alpha, \beta] = [\pi/3, \pi/3]$ and $(h, \Delta) = (1, 1/2)$ falling inside the TSF in Fig.2.

2. *Method 2:* Eq.D1 can also be written as

$$\Omega_n(k) = - \sum_{n' \neq n} \frac{2\text{Im}[\langle \psi_{nk} | (\partial_x H_k) | \psi_{n'k} \rangle \langle \psi_{n'k} | (\partial_y H_k) | \psi_{nk} \rangle]}{(\omega_{n'} - \omega_n)^2} \quad (D3)$$

Setting $[\alpha, \beta] = [\pi/3, \pi/3]$. When $(h, \Delta) = (1, 1/2)$ falling in the TSF, $C_1 = -1.63415 \times 10^{-12} = 0$, $C_2 = 2.000000000001559 = 2$.

When $(h, \Delta) = (1, 2)$ falling in the SF, $C_1 = 2.15106 \times 10^{-16} = 0$, $C_2 = 5.99347 \times 10^{-16} = 0$.

When $(h, \Delta) = (4, 1/2)$ falling in the BI, $C_1 = 3.06829 \times 10^{-16} = 0$, $C_2 = -2.31586 \times 10^{-16} = 0$.

3. *Method 3:* This method was designed in⁵⁰ to give exact integer Chern numbers. One first define a U(1) link variable from the wave functions of the n -th band as:

$$U_\mu(k_l) = \langle \psi_n(k_l) | \psi_n(k_l + \hat{\mu}_i) \rangle / |\langle \psi_n(k_l) | \psi_n(k_l + \hat{\mu}_i) \rangle| \quad (D4)$$

where $\hat{\mu}_i$ is a vector in the direction $i = x, y$ with the magnitude $2\pi/N_i$. Then one define a lattice field strength as,

$$F_{xy}(k_l) = \ln[U_x(k_l)U_y(k_l + \mu_x)U_x(k_l + \mu_y)^{-1}U_y(k_l)^{-1}] \quad (D5)$$

where the principal branch of the logarithm is with, $-\pi < F_{xy}/i \leq \pi$. The Chern number associated to the band ω_n is given by,

$$C_n = \frac{i}{2\pi} \sum_l F_{xy}(k_l) \quad (D6)$$

It is a very efficient method. Within 10 seconds on a conventional laptop, we obtain $C_1 = 0$, $C_2 = 2$, $C_3 = -2$ and $C_4 = 0$ when $(h, \Delta) = (1, 1/2)$ falling in the TSF.

We also used the three methods to calculate the Berry curvature using the 2 bands effective actions in Eq.2,6 and Eq.C1 and found they reproduce those from the original four bands theory shown in Fig.3, 4 and 8 very precisely.

Appendix E: The spin and spatial structure of the Edge states in the $C = 2$ TSF and bulk-edge correspondences.

1. Edge state near h_{c1} .

To get the edge modes near h_{c1} , we set $q_x \rightarrow -i\partial_x, q_y \rightarrow -i\partial_y$ in Eq.2. For the edge at $x = 0$ shown in Fig.2, the momentum k_y remains a good quantum number, one need to solve $H_{E, h_{c1}} \psi(x) = E\psi(x)$. Setting $q_y = 0$ and $E = 0$ leads to

$$\left[\left(\delta h - \frac{t^2 \cos^2 \alpha \partial_x^4}{2\Delta} \right) \sigma_3 - i2t \sin \alpha \partial_x \sigma_1 \right] \psi(x) = 0 \quad (E1)$$

with the edge state wavefunction $\psi(x) = \begin{bmatrix} \psi_1 \\ \psi_2 \end{bmatrix} e^{\lambda x}$. The corresponding eigen-value equation

$$\delta h - \frac{t^2 \cos^2 \alpha \lambda^4}{2\Delta} + 2t \sin \alpha \lambda = 0 \quad (E2)$$

has 4 roots. When $\delta h > 0$ is small, the only physically relevant root is $\lambda = -\delta h / 2t \sin \alpha$.

By imposing the additional Majorana fermion condition $u_{k_y}^*(x) = -v_{-k_y}(x)$, one find the $q_y = 0$ edge state wavefunction:

$$\begin{bmatrix} u_0(x) \\ v_0(x) \end{bmatrix} = iR \begin{bmatrix} e^{-i\frac{\pi}{4}} \\ e^{i\frac{\pi}{4}} \end{bmatrix} e^{-\lambda x} \quad (E3)$$

where $l_d^{-1} = \lambda = -\delta h / 2t \sin \alpha$ is the inverse length decaying into the bulk and $R = \sqrt{\lambda}$ is the normalization constant. When comparing to the bulk energy spectrum Eq.5, one can see that the decaying length $l_d^{-1} = \Delta / v_f$ where $\Delta = \delta h$ is the minimum bulk gap and $v_f = 2t \sin \alpha$ is the edge velocity. This could be the simplest the

bulk-edge correspondence. The above procedures can be extended to derive the wavefunction at any given $k_y = \pi + q_y$ with the eigen-energy $E = v_f q_y$ where $v_f = 2t \sin \alpha$.

The notable feature here is that Eq.2 is not isotropic in (q_x, q_y) , so the edge state depends on orientation of the edge. Setting $\tilde{q}_x = (q_x - q_y)/\sqrt{2}$, $\tilde{q}_y = (q_x + q_y)/\sqrt{2}$, then making simultaneous rotation in the spin space, Eq.2 can be rewritten as:

$$\tilde{H}_{(0,\pi)} = \left(\delta h - \frac{t^2 \cos^2 \alpha \tilde{q}_x^2 \tilde{q}_y^2}{\Delta} \right) \sigma_3 + 2t \sin \alpha (\tilde{q}_x \tilde{\sigma}_1 + \tilde{q}_y \tilde{\sigma}_2) \quad (\text{E4})$$

So the edge state along the edge $\tilde{x} = 0$ (or $x = \pm y$) can be similarly constructed in the rotated basis as above.

In the expression of $\phi_{L\mathbf{k}}$ listed above Eq.2, k_y remain good quantum number, setting $k_x \rightarrow x$ leads to the edge operator at a given k_y :

$$c_{2L,k_y}(x) = \frac{1}{\sqrt{2}} \begin{bmatrix} c_{-k_y\uparrow}^\dagger(x) - c_{k_y\downarrow}(x) \\ c_{-k_y\downarrow}^\dagger(x) - c_{k_y\uparrow}(x) \end{bmatrix} \quad (\text{E5})$$

We get the Majorana edge mode $\gamma_2(k_y)$ in Eq.8:

$$\begin{aligned} \gamma_2(k_y) &= \frac{1}{\sqrt{2}} \int_0^\infty dx \left[(u_{k_y}^*(x) c_{-k_y\uparrow}^\dagger(x) - v_{k_y}^*(x) c_{k_y\uparrow}(x)) \right. \\ &\quad \left. + (v_{k_y}^*(x) c_{-k_y\downarrow}^\dagger(x) - u_{k_y}^*(x) c_{k_y\downarrow}(x)) \right] \\ &= \gamma_{2\uparrow}(k_y) + \gamma_{2\downarrow}(k_y) \end{aligned} \quad (\text{E6})$$

which satisfies $\gamma_2^\dagger(k_y) = \gamma_2(-k_y)$ and includes both spin up $\gamma_{2\uparrow}(k_y)$ in the first line and the spin down $\gamma_{2\downarrow}(k_y)$ in the second line.

Similarly, using the effective action $H_{(\pi,0)}$, one can derive the Majorana edge mode $\gamma_1(k_y)$ near $k_y = 0$ in Eq.8. Because the unitary transformation $S_{(\pi,0)} = S_{(0,\pi)}$, so the form of Eq.E5 and Eq.E6 hold also for $\gamma_1(k_y)$.

2. Edge state near h_{c2}

To get the edge modes along a edge at $x = 0$ near h_{c2} , we set $q_x \rightarrow -i\partial_x$ in Eq.6. Similar procedures as in⁴ can be used to find the edge mode at a given k_y near h_{c2} by imposing the additional Majorana fermion condition $u_{k_y}^*(x) = -v_{-k_y}(x)$. The $k_y = 0$ energy eigenvalue equation near h_{c1} is:

$$M + B\lambda^2 + A\lambda = 0 \quad (\text{E7})$$

where as written below Eq.6: $A = \frac{\Delta \tan \alpha}{2}$, $B = t \frac{1+\cos^2 \alpha}{2 \cos \alpha}$, $M = \delta h$.

One salient feature here is that both A and M are critical near h_{c2} . By a simple GL analysis, $\Delta \sim (\delta h)^{1/2}$, so, in general, $D = A^2 - 4MB$ could be either positive or negative. However, as shown in the Sec.V and Fig.4, it is negative here, so Eq.E7 has the two physical roots with negative real part:

$$\lambda_{3,4} = -\frac{A \pm i\sqrt{|D|}}{2B} \quad (\text{E8})$$

which we denote by $\lambda_3, \lambda_4 = \lambda_3^*$.

After imposing the additional hard boundary condition $\psi(x=0) = 0$, we can find a unique $E = 0$ edge state wavefunction:

$$\begin{bmatrix} u_0(x) \\ v_0(x) \end{bmatrix} = iR \begin{bmatrix} -e^{i\frac{\pi}{4}} \\ e^{i\frac{\pi}{4}} \end{bmatrix} (e^{\lambda_3 x} - e^{\lambda_3^* x}) \quad (\text{E9})$$

where $R = \sqrt{\frac{|Re\lambda_3||\lambda_3|^2}{2(|Re\lambda_3|^2 + |\lambda_3|^2)}}$ is the normalization constant.

The magnitude of the wavefunction $|\Phi(x)|^2$ Eq.E9 decays into the bulk with the decaying length $l_d^{-1} = |Re\lambda_3| = A/2B$ with oscillating period $l_o^{-1} = |Im\lambda_3| = \sqrt{|D|}/2B$ which is consistent with the decaying-oscillating behaviors in the ED study in Fig.5. Again, the above procedures can be extended to derive the wavefunction at any given k_y with the eigen-energy $E = v_f q_y$ where $v_f = A$. When comparing with the bulk energy spectrum Eq.7, we find that it is the oscillating length $l_o^{-1} = E_{min}/v_f$ which can be expressed as the minimum bulk gap over the edge velocity, while the decay length $l_d^{-1} = E_{min}/\sqrt{|D|}$ is more complicated than that near h_{c1} . Because $\sqrt{|D|} > A$, so $l_o < l_d$ which is consistent with Fig.5a.

In the expression of $\phi_{L\mathbf{k}}$ listed below Eq.6, setting $k_x \rightarrow x$ leads to the edge operator at a given k_y :

$$c_{3L,k_y}(x) = \begin{bmatrix} c_{-k_y\downarrow}^\dagger(x) \\ c_{k_y\downarrow}(x) \end{bmatrix} \quad (\text{E10})$$

which contains only spin down. The Majorana edge mode is given by:

$$\gamma_3(k_y) = \int dx \left[u_{k_y}^*(x) c_{-k_y\downarrow}^\dagger(x) + v_{k_y}^*(x) c_{k_y\downarrow}(x) \right] \quad (\text{E11})$$

which satisfies $\gamma_3^\dagger(k_y) = \gamma_3(-k_y)$ and includes the only spin down.

Similarly, using the effective action $H_{(\pi,\pi)}$, one find the Majorana fermion near $k_y = \pi$:

$$c_{4L,k_y}(x) = \begin{bmatrix} c_{k_y\uparrow}(x) \\ c_{-k_y\uparrow}^\dagger(x) \end{bmatrix} \quad (\text{E12})$$

which contains only spin up and

$$\gamma_4(k_y) = \int dx \left[u_{k_y}^*(x) c_{k_y\uparrow}(x) + v_{k_y}^*(x) c_{-k_y\uparrow}^\dagger(x) \right] \quad (\text{E13})$$

which satisfies $\gamma_4^\dagger(k_y) = \gamma_4(-k_y)$ and includes the only spin up.

Appendix F: Spin structure of the Majorana zero modes in the vortex core of the $C = 2$ TSF

We can still use the effective action Eq.2 near $(\pi, 0)$ and $(0, \pi)$ to study analytically the Majorana zero modes inside a vortex core near h_{c1} . The main procedures are

outlined in Sec.VII. Here we list the explicit expressions of the Majorana zero modes. The edge-vortex core correspondence was also discussed in Sec.VII.

1. *Two Majorana zero modes γ_1, γ_2 near h_{c1} :*

In the expression of $\phi_{L\mathbf{k}}$ listed above Eq.5, setting $\mathbf{k} \rightarrow \mathbf{r}$ leads to the particle operator at a given \mathbf{r} :

$$c_{2L}(\mathbf{r}) = \frac{1}{\sqrt{2}} \begin{bmatrix} c_{\uparrow}^{\dagger}(\mathbf{r}) - c_{\downarrow}(\mathbf{r}) \\ c_{\downarrow}^{\dagger}(\mathbf{r}) - c_{\uparrow}(\mathbf{r}) \end{bmatrix} \quad (\text{F1})$$

which contain both spin up and spin down. It can be fused with the zero-mode wavefunctions $(u(\mathbf{r}), v(\mathbf{r}))$ to lead to the Majorana zero mode γ_2 in Eq.10:

$$\begin{aligned} \gamma_2 &= \frac{1}{\sqrt{2}} \int d\mathbf{r} [(u^*(\mathbf{r})c_{\uparrow}^{\dagger}(\mathbf{r}) - v^*(\mathbf{r})c_{\uparrow}(\mathbf{r})) \\ &\quad + (v^*(\mathbf{r})c_{\downarrow}^{\dagger}(\mathbf{r}) - u^*(\mathbf{r})c_{\downarrow}(\mathbf{r}))] \\ &= \gamma_{2\uparrow} + \gamma_{2\downarrow} \end{aligned} \quad (\text{F2})$$

which satisfies $\gamma_2^{\dagger} = \gamma_2, \gamma_2^2 = 1/2$ and includes both spin up $\gamma_{2\uparrow}, \gamma_{2\uparrow}^2 = 1/4$ in the first line and the spin down $\gamma_{2\downarrow}, \gamma_{2\downarrow}^2 = 1/4$ in the second line.

Similarly, using the effective action $H_{(\pi,0)}$ near $(\pi, 0)$, one can derive another Majorana zero mode γ_1 which take a similar form as Eq.F2. So a single vortex contains two Majorana zero modes γ_1, γ_2 .

2. *Two Majorana zero modes γ_3, γ_4 near h_{c2} .*

Eq.F1 should be replaced by:

$$c_{3L}(\mathbf{r}) = \begin{bmatrix} c_{\downarrow}^{\dagger}(\mathbf{r}) \\ c_{\downarrow}(\mathbf{r}) \end{bmatrix} \quad (\text{F3})$$

which contains only spin down, Eq.F2 should be replaced by:

$$\gamma_3 = \int d\mathbf{r} [u^*(\mathbf{r})c_{\downarrow}^{\dagger}(\mathbf{r}) + v^*(\mathbf{r})c_{\downarrow}(\mathbf{r})] \quad (\text{F4})$$

which satisfies $\gamma_3^{\dagger} = \gamma_3, \gamma_3^2 = 1/2$ and includes the only spin down.

When using the effective action $H_{(\pi,\pi)}$, one can derive another Majorana zero mode γ_4 :

$$c_{4L}(\mathbf{r}) = \begin{bmatrix} c_{\uparrow}^{\dagger}(\mathbf{r}) \\ c_{\uparrow}(\mathbf{r}) \end{bmatrix} \quad (\text{F5})$$

which contains only spin up and

$$\gamma_4 = \int d\mathbf{r} [u^*(\mathbf{r})c_{\uparrow}(\mathbf{r}) + v^*(\mathbf{r})c_{\uparrow}^{\dagger}(\mathbf{r})] \quad (\text{F6})$$

which satisfies $\gamma_4^{\dagger} = \gamma_4, \gamma_4^2 = 1/2$ and includes the only spin up.

-
- ¹ X.G. Wen and Q. Niu, Phys. Rev. B41, 9377 (1990); Wen, X. G. Quantum Field Theory of Many-body Systems (Oxford University Press, 2004).
- ² Volovik, G. E. The Universe in a Helium Droplet (Oxford University Press, USA, 2003).
- ³ M. Z. Hasan and C. L. Kane, Colloquium: Topological insulators, Rev. Mod. Phys. **82**, 3045 (2010).
- ⁴ X. L. Qi and S. C. Zhang, Topological insulators and superconductors, Rev. Mod. Phys. **83**, 1057 (2011).
- ⁵ S. Sachdev, *Quantum Phase transitions*, (2nd edition, Cambridge University Press, 2011).
- ⁶ L. Savary and L. Balents, *Quantum Spin liquids*, arXiv:1601.03742 (2016).
- ⁷ Fa-Di Sun, Xiao-Lu Yu, Jinwu Ye, Heng Fan, W. M. Liu, Scientific Reports 3, 2119 (2013), Topological Quantum Phase Transition in Synthetic Non- Abelian Gauge Potential: Gauge Invariance and Experimental Detections.
- ⁸ Masatoshi Sato, Yoshiro Takahashi, and Satoshi Fujimoto, Phys. Rev. Lett. 103, 020401 C Published 6 July 2009
- ⁹ Jay D. Sau, Roman M. Lutchyn, Sumanta Tewari, and S. Das Sarma, Phys. Rev. Lett. 104, 040502 C Published 27 January 2010; Roman M. Lutchyn, Jay D. Sau, and S. Das Sarma, Phys. Rev. Lett. 105, 077001 C Published 13 August 2010; Parag Ghosh, Jay D. Sau, Sumanta Tewari, and S. Das Sarma, Phys. Rev. B 82, 184525 C Published 16 November 2010; Jay D. Sau, Sumanta Tewari, Roman M. Lutchyn, Tudor D. Stanescu, and S. Das Sarma, Phys. Rev. B 82, 214509 C Published 9 December 2010
- ¹⁰ Jason Alicea, Phys. Rev. B 81, 125318 C Published 15 March 2010
- ¹¹ Immanuel Bloch, Jean Dalibard, and Wilhelm Zwerger, Many-body physics with ultracold gases, Rev. Mod. Phys. 80, 885 C Published 18 July 2008.
- ¹² Lianghai Huang, *et.al*, Experimental realization of a two-dimensional synthetic spin-orbit coupling in ultracold Fermi gases, Nature Physics 12, 540-544 (2016).
- ¹³ Zengming Meng, *et.al*, Experimental observation of topological band gap opening in ultracold Fermi gases with two-dimensional spin-orbit coupling, arXiv:1511.08492.
- ¹⁴ Zhan Wu, *et.al*, Realization of Two-Dimensional Spin-orbit Coupling for Bose-Einstein Condensates, arXiv:1511.08170
- ¹⁵ Michael L. Wall, *et.al*, Synthetic Spin-Orbit Coupling in an Optical Lattice Clock, Phys. Rev. Lett. 116, 035301 (2016).
- ¹⁶ Nathaniel Q. Burdick, Yijun Tang, and Benjamin L. Lev, Long-Lived Spin-Orbit-Coupled Degenerate Dipolar Fermi Gas, Phys. Rev. X 6, 031022 C Published 17 August 2016.
- ¹⁷ I. Bloch, J. Dalibard, and W. Zwerger, Rev. Mod. Phys. 80, 885 (2008).
- ¹⁸ Medley, P., Weld, D. M., Miyake, H., Pritchard, D. E. & Ketterle, W. Spin Gradient Demagnetization Cooling of Ultracold Atoms. *Phys. Rev. Lett.* **106**, 195301 (2011).
- ¹⁹ Sugawa, S. *et al*. Interaction and filling-induced quantum phases of dual Mott insulators of bosons and fermions. *Nat. Phys.* **7**, 642 (2011).
- ²⁰ J. T. Stewart, J. P. Gaebler and D. S. Jin, Using photoemission spectroscopy to probe a strongly interacting Fermi gas, Nature 454, 744-747 doi:10.1038/nature07172.
- ²¹ Christian H. Schunck¹, Yong-il Shin¹, Andr Schirotzek, Wolfgang Ketterle, Determination of the fermion pair size

- in a resonantly interacting superfluid, *Nature* 454, 739-743 (7 August 2008).
- ²² Leticia Tarruell, Daniel Greif, Thomas Uehlinger, Gregor Jotzu and Tilman Esslinger, Creating, moving and merging Dirac points with a Fermi gas in a tunable honeycomb lattice, *Nature* 483, 302-305 doi:10.1038/nature10871.
 - ²³ M. Aidelsburger, M. Lohse, C. Schweizer, M. Atala, J. T. Barreiro, S. Nascimbe, N. R. Cooper, I. Bloch and N. Goldman, *Measuring the Chern number of Hofstadter bands with ultracold bosonic atoms*, *Nat. Phys.* advance online publication: 22 DECEMBER 2014 (DOI: 10.1038/NPHYS3171).
 - ²⁴ N. Goldman, J. Dalibard, A. Dauphin, F. Gerbier, M. Lewenstein, P. Zoller, I. B. Spielman, Direct imaging of topological edge states in cold-atom systems, *PNAS* 110(17) 6736-6741 (2013).
 - ²⁵ Gemelke, N., Zhang X., Huang C. L., and Chin, C. In situ observation of incompressible Mott-insulating domains in ultracold atomic gases, *Nature (London)* **460**, 995 (2009).
 - ²⁶ We expect that the Pfaffian defined from the two discrete symmetries respectively at the four momenta are identical. It was known³ that the Pfaffian is equal to the parity of the Chern number. Because, the TSF in Fig.1 has Chern number $C = 2$, so the Pfaffian can not be used to distinguish the trivial SF with $C = 0$ and the TSF with $C = 2$ in Fig.1.
 - ²⁷ In the context of topological quantum computing, a Dirac fermion is useless, but it is well known that a single Majorana fermion is not useful for universal topological quantum computing either.
 - ²⁸ Yi-Xiang Yu, Jinwu Ye, Wu-Ming Liu, Coherent lengths in attractively interacting Fermi gases with Spin-orbit Couplings, *Phys. Rev. A* 90, 053603 (2014).
 - ²⁹ Jinwu Ye and S. Sachdev, The effects of Coulomb interaction on Quantum Hall critical points of systems in a periodic potential, *Phys. Rev. Lett.* 80, 5409 (1998).
 - ³⁰ Jinwu Ye, The effects of weak disorders and Coulomb interaction on Quantum Hall critical points, *Phys. Rev. B* 60, 8290 (1999).
 - ³¹ Fadi Sun, Jinwu Ye, Wu-Ming Liu, Quantum magnetism of spinor bosons in optical lattices with synthetic non-Abelian gauge fields at zero and finite temperatures, *Phys. Rev. A* 92, 043609 (2015).
 - ³² Fadi Sun, Jinwu Ye, Wu-Ming Liu, Classification of magnons in Rotated Ferromagnetic Heisenberg model and their competing responses in transverse fields, *Phys. Rev. B* 94, 024409 (2016).
 - ³³ Fadi Sun, Jinwu Ye, Wu-Ming Liu, Hubbard model with Rashba or Dresselhaus spin-orbit coupling and Rotated Anti-ferromagnetic Heisenberg Model, arXiv:1601.01642, to be published in *Phys. Rev. B*.
 - ³⁴ Fadi Sun, Jinwu Ye, Wu-Ming Liu, *Quantum incommensurate Skyrmion crystals and Commensurate to Incommensurate transitions in cold atoms and materials with strong spin orbit couplings*, arXiv:1502.05338.
 - ³⁵ N. Read and Dmitry Green, *Phys. Rev. B* 61, 10267 C Published 15 April 2000
 - ³⁶ Here, we are using the normalization $\{\gamma_i, \gamma_j\} = \delta_{ij}$ instead of the more conventional one $\{\gamma_i, \gamma_j\} = 2\delta_{ij}$ which seems more natural in the BdG equation normalization.
 - ³⁷ Jinwu Ye, *Phys. Rev. Lett.* 77, 3224 (1996); *Phys. Rev. Lett.* 79, 1385 (1997).
 - ³⁸ See P. Ghaemi and F. Wilczek, arXiv:0709.2626; D.L. Bergman and K Le Hur *Phys. Rev. B* 79, 184520 (2009).
 - ³⁹ Jinwu Ye, *Phys. Rev. Lett.* 86, 316 (2001); *Phys. Rev. Lett.* 87, 227003 (2001); *Phys. Rev. B* 65, 214505 (2002).
 - ⁴⁰ Yu Yi-Xiang, Fadi Sun, Jinwu Ye and Ningfang Song, unpublished.
 - ⁴¹ In fact, by using the unitary transformation $U = e^{i\pi/2\sigma_z}$, one can reach the same Hamiltonian with the corresponding transformation in the two component spinor ϕ_L .
 - ⁴² Longhua Jiang and Jinwu Ye, *J. Phys, Condensed Matter*. 18 (2006) 6907-6922
 - ⁴³ Jinwu Ye, *Nucl. Phys. B* 805 (3) 418-440 (2008).
 - ⁴⁴ Yan Chen and Jinwu Ye, *Philos. Mag.* 92 (2012) 4484-4491; *Nucl. Phys. B* 869 (2013), 242-281.
 - ⁴⁵ M. Takahashi, Half filled Hubbard model at low temperature, *J. Phys, C. Solid State Phys.* 10, 1289 (1977).
 - ⁴⁶ Longhua Jiang and Jinwu Ye, *Phys. Rev. B* 76, 184104 (2007); Jinwu Ye, *J. Low Temp Phys.* 160(3), 71-111, (2010).
 - ⁴⁷ V. Schweikhard, I. Coddington, P. Engels, V. P. Mogen-dorff, and E. A. Cornell, Rapidly Rotating Bose-Einstein Condensates in and near the Lowest Landau Level, *Phys. Rev. Lett.* 92, 040404 (2004).
 - ⁴⁸ Yu Yi-Xiang, Jinwu Ye and W.M. Liu, *Scientific Reports* 3, 3476 (2013).
 - ⁴⁹ R. Jackiw and C. Rebbi, *Phys. Rev. D* 13, 3398 (1976).
 - ⁵⁰ Takahiro FUKUI, *Journal of the Physical Society of Japan*, Vol. 74, No. 6, June, 2005, pp. 1674-1677.
 - ⁵¹ J. Ye and S. Sachdev, *Phys. Rev. B* 44, 10173 (1991).
 - ⁵² The chemical potential means the Fermi energy only in the normal phase where $\Delta = 0$. However, when inside a SF, the particle number is not conserved, it can only be used to determine the average particle number.
 - ⁵³ Shang-Shun Zhang, Jinwu Ye, Wu-Ming Liu, Itinerant magnetic phases and Quantum Lifshitz transitions in repulsively interacting spin-orbit coupled Fermi gas, *Phys. Rev. B* 94, 115121 (2016).
 - ⁵⁴ Fadi Sun, Jinwu Ye, Wu-Ming Liu, arXiv:1603.00451.
 - ⁵⁵ It was known that the finite momentum η pairing in the negative U Hubbard model is mapped to a FM in XY plane in the positive U case by a particle-hole transformation.